

This is the accepted version of the article:

Masvidal-Codina E., Illa X., Dasilva M., Calia A.B., Dragojevic T., Vidal-Rosas E.E., Prats-Alfonso E., Martínez-Aguilar J., De la Cruz J.M., Garcia-Cortadella R., Godignon P., Rius G., Camassa A., Del Corro E., Bousquet J., Hébert C., Durduran T., Villa . High-resolution mapping of infraslow cortical brain activity enabled by graphene microtransistors. *Nature Materials*, (2019). 18. : 280 - . 10.1038/s41563-018-0249-4.

Available at: <https://dx.doi.org/10.1038/s41563-018-0249-4>

High-resolution mapping of infraslow cortical brain activity enabled by graphene microtransistors

Eduard Masvidal-Codina¹, Xavi Illa^{2,1}, Miguel Dasilva³, Andrea Bonaccini Calia⁴, Tanja Dragojević⁵, Ernesto E. Vidal-Rosas⁵, Elisabet Prats-Alfonso^{2,1}, Javier Martínez-Aguilar^{1,2}, Jose M. De la Cruz Sanchez⁴, Ramon Garcia-Cortadella⁴, Philippe Godignon¹, Gemma Rius¹, Alessandra Camassa³, Elena Del Corro⁴, Jessica Bousquet⁴, Clement Hébert⁴, Turgut Durduran^{5,6}, Rosa Villa^{1,2}, Maria V Sanchez-Vives^{3,6}, Jose A Garrido^{4,6*} and Anton Guimerà-Brunet^{1,2*}

1 Institut de Microelectrònica de Barcelona, IMB-CNM (CSIC), Esfera UAB, Bellaterra, Spain

2 Centro de Investigación Biomédica en Red en Bioingeniería, Biomateriales y Nanomedicina (CIBER-BBN), Madrid, Spain

3 Institut d'Investigacions Biomèdiques August Pi i Sunyer (IDIBAPS), Barcelona, Spain

4 Catalan Institute of Nanoscience and Nanotechnology (ICN2), CSIC and The Barcelona Institute of Science and Technology (BIST), Campus UAB, Bellaterra, Barcelona, Spain

5 ICFO-Institut de Ciències Fotòniques, The Barcelona Institute of Science and Technology, Castelldefels, Barcelona, Spain

6 Institució Catalana de Recerca i Estudis Avançats (ICREA), Barcelona, Spain

* Correspondence:

anton.guimera@imb-cnm.csic.es; joseantonio.garrido@icn2.cat

Keywords: cortical spreading depression, DC-ECOG, graphene, infraslow.

1 **Abstract**

2 Recording infraslow brain signals (< 0.1 Hz) with microelectrodes is severely hampered by current
3 microelectrode materials, primarily due to limitations resulting from voltage drift and high electrode
4 impedance. Hence, most recording systems include high-pass filters that solve saturation issues but
5 come in hand with loss of physiological and pathological information. In this work, we use flexible
6 epicortical and intracortical arrays of graphene solution-gated field-effect transistors (gSGFETs) to
7 map cortical spreading depression in rats and demonstrate that gSGFETs are able to record, with
8 high-fidelity, infraslow signals together with signals in the typical local field potential bandwidth.
9 The wide recording bandwidth results from the direct field-effect coupling of the active transistor, in
10 contrast to standard passive electrodes, as well as from the electrochemical inertness of graphene.
11 Taking advantage of such functionality, we envision broad applications of gSGFET technology for
12 monitoring infraslow brain activity both in research and in the clinic.

13 Recently, there has been a particular resurgence of interest in fluctuations of brain activity occurring
14 at < 0.1 Hz, commonly referred to as very slow, ultraslow or infralow activity (ISA)¹. ISA is
15 suggested to have a unique neurophysiological basis², and to be indicative of brain states (e.g. sleep,
16 anesthesia, coma, wakefulness)²⁻⁴. ISA is also correlated with resting-state networks in functional
17 magnetic resonance imaging⁵ and may significantly contribute to the high variability observed in the
18 time course of physiological signals^{6,7}. Interestingly, cortical spreading depression (CSD)^{8,9}, a slowly
19 propagating wave of near-complete depolarization of neurons and astrocytes followed by a period of
20 electrical activity suppression, occurs at infralow frequencies. CSD is often triggered in individuals
21 suffering stroke or brain injury as well as migraines and recent research has shown that CSD plays a
22 significant role in brain pathophysiology¹⁰⁻¹². For this reason, monitoring electrophysiological signals
23 below 0.1 Hz can be very valuable for clinical diagnosis, prognosis and therapy in neurocritical
24 care¹³⁻¹⁵.

25 Non-invasive techniques such as electroencephalography (EEG) and magnetoencephalography
26 (MEG) have been used to study ISA^{16,17}. However, their limited spatial resolution, and averaged
27 signal impose serious limitations, e.g. scalp EEG alone is not sufficient for CSD detection^{14,18}.
28 Hence, invasive electrophysiological techniques are the most widely used to record infralow
29 brainwaves. The proper recording of ISA requires the use of direct-coupled amplifiers and extremely
30 stable and low-impedance invasive electrodes. Traditionally, liquid-filled glass micropipettes are
31 used, which allow only one or few-point measurements¹⁹ and therefore impose serious mapping
32 limitations. For higher spatial resolution and mapping, non-polarizable silver/silver chloride
33 (Ag/AgCl) electrodes could be used, which prevent charge accumulation at the interface and
34 therefore voltage drift. However, due to the toxicity of silver, the use of such electrodes for human or
35 chronic animal *in vivo* monitoring is not an option²⁰. This has fostered the search for alternative
36 microelectrode materials with low impedance and drift, although none has yet been found capable of
37 offering performance comparable to Ag/AgCl electrodes²¹. Current ISA recordings in humans are
38 performed with platinum electrodes, which challenge CSD detection due to artefacts and transients¹³.
39 Moreover, miniaturization of electrode size to achieve higher spatial resolution may cause intrinsic
40 high-pass filtering of ISA due to the associated electrode impedance increase^{22,23}. Other invasive
41 optical techniques, such as calcium imaging are also used to monitor ISA, but still nowadays they
42 present serious challenges in resolving high-frequency activity for a large number of neurons^{24,25} and
43 their intrinsic need of indicators limits the translation to clinical use. Consequently, there is a
44 pressing need for a technique that allows measuring large-scale, high-spatiotemporal resolution
45 electrophysiological signals including infralow frequencies in a potentially fully implantable,
46 nontoxic, clinical-scale system. (Table S1).

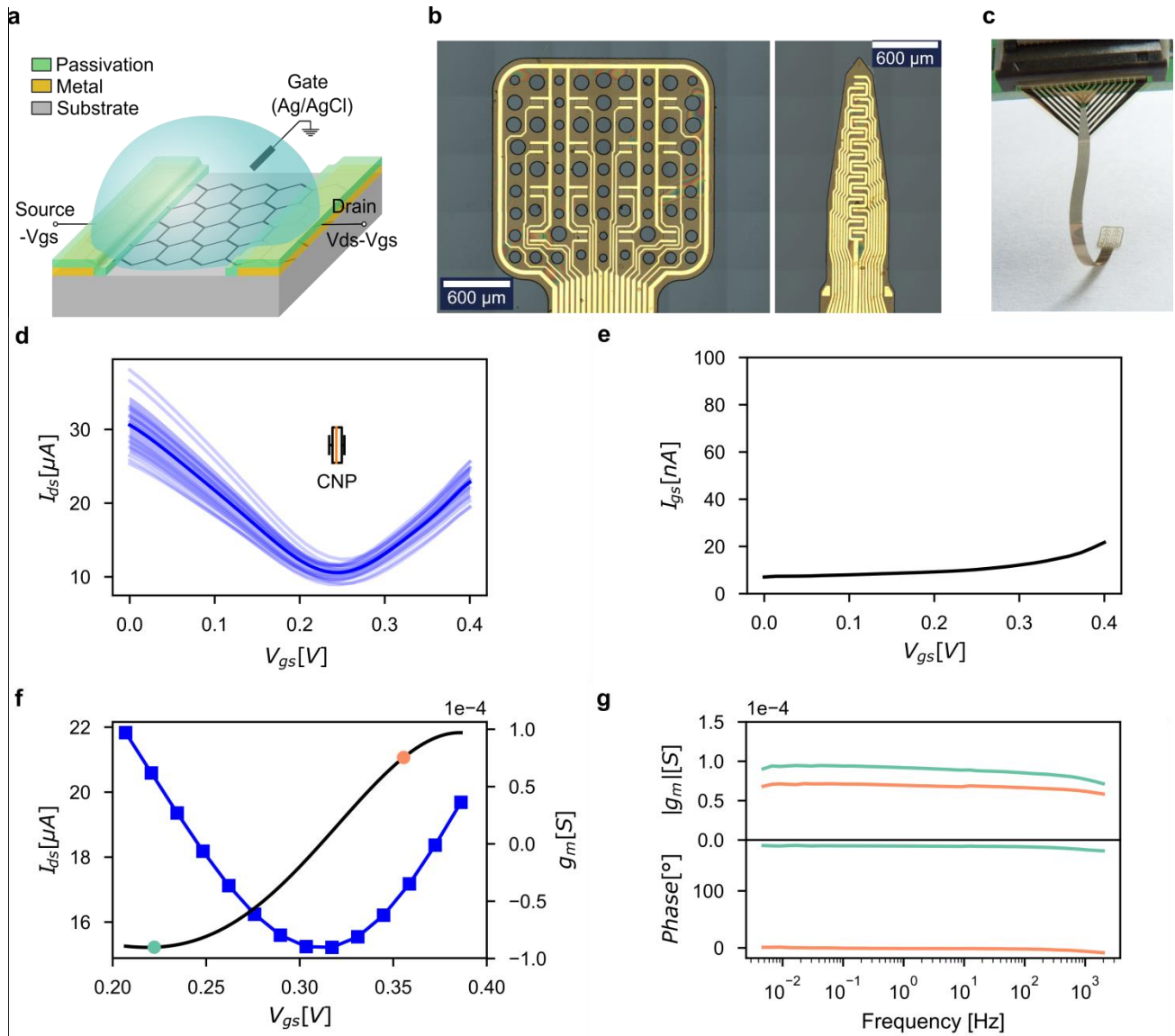
47 As an alternative to the commonly used microelectrode technology, recording electrophysiological
48 signals with field-effect transistors (FETs) offers several advantages: they are less sensitive to
49 environmental noise thanks to their intrinsic voltage-to-current amplification, and they can be easily
50 multiplexed²⁶. Nonetheless, the difficulties in combining high gate capacitance and carrier mobility
51 silicon FETs with flexible materials has historically hampered their use for *in vivo* recordings²⁷.
52 Graphene solution-gated field-effect transistors (gSGFETs) have been proposed to potentially
53 overcome most previous drawbacks²⁸. Graphene flexibility allows gSGFETs to be embedded in ultra-

54 soft and flexible substrates without loss of performance²⁹, while its wide electrochemical window and
55 biocompatibility allows direct contact with biological fluids and tissues and ensures a safe operation
56 in *in vivo* conditions³⁰. In addition, the two-dimensional nature of graphene provides the highest
57 surface-to-volume ratio possible, making graphene very sensitive to charges at its surface. Taking
58 advantage of the above-mentioned properties, in previous works, we demonstrated that gSGFETs are
59 able to record local field potentials^{31,32}.

60 In this work, we investigate the potential of graphene microtransistors to record infraslow brain
61 activity by performing *in vivo* recordings where we use, gSGFETs for both epicortical and
62 intracortical mapping of cortical spreading depression. We found that graphene microtransistors are
63 excellent devices for recording infraslow signals, performing similarly to solution-filled glass
64 micropipettes while additionally offering the possibility of performing spatially-resolved mapping.
65 Importantly, gSGFETs do not compromise the acquisition of signals in the conventional local field
66 potential bandwidth, therefore allowing recording in a wide frequency bandwidth. Furthermore, we
67 also demonstrate that gSGFET technology can be used in combination with optical techniques, such
68 as laser speckle contrast imaging, to obtain 2-D maps of neurovascular coupling.

69 **Fabrication and characterization of gSGFET arrays**

70 A gSGFET is a device in which graphene is used as channel material, contacted by two metal leads
71 (source and drain terminals), in direct contact with an electrolyte solution or conductive biological
72 tissue where a reference electrode is placed and used as gate terminal (Fig. 1a). We fabricated 12 μm -
73 thick flexible probes containing arrays of gSGFETs in both epicortical and intracortical designs (Fig.
74 1b) using the process previously reported³². The arrays were placed in zero insertion force connectors
75 for interfacing with recording electronics (Fig. 1c). Characterization consisted in measuring the
76 transfer curve, drain current (I_{ds}) vs gate-source voltage (V_{gs}), of all gSGFETs in each array with a
77 fixed drain-source voltage (V_{ds}). The small dispersion of the charge neutrality point obtained
78 (CNP= 243.6 ± 6.1 mV), which is defined as the V_{gs} voltage associated to the minimum current value
79 of the transfer curve, indicates the homogeneity of the transistors (Fig. 1d). Importantly, since V_{gs} and
80 V_{ds} are shared, a small CNP dispersion allows near-optimal recording performance for all gSGFETs
81 in the same array. The leakage current (I_{gs}) for all gSGFETs in the array was also measured, being in
82 the nA range throughout the voltage sweep (Fig. 1e), demonstrating the good insulation of the
83 passivation layer and the negligible reactivity of the graphene. Furthermore, we measured the
84 frequency response of the transconductance (g_m), which indicates the efficiency of the signal
85 coupling ($\partial I_{ds}/\partial V_{gs}$). The negative g_m for V_{gs} values lower than the CNP results in an inversion
86 (180° phase) of the signals measured at such bias while for V_{gs} values higher than the CNP the signal
87 phase is preserved. In both cases, we obtained constant g_m values in a wide bandwidth (Fig. 1f-g).



88

89 **Fig. 1 | Flexible graphene solution-gated field-effect transistor array technology and characterization.** **a,**
 90 Schematic of a graphene transistor polarized in common gate mode. **b,** Optical microscope images of the
 91 active area of a 4×4 gSGFET array and a 15 channel intracortical array. **c,** Photograph of the neural probe after
 92 peeling from the wafer and being introduced into a zero insertion force connector. **d-g,** Steady-state and
 93 frequency response characterization of a 100x50-μm² gSGFET array in 10 mM phosphate buffered saline
 94 (PBS) with a drain-source voltage bias (V_{ds}) of 50 mV. **d,** gSGFET transfer curves (blue lines), drain-source
 95 current (I_{ds}) vs gate-source voltage (V_{gs}), together with the mean (dark blue) and standard deviation (blue
 96 shade). Boxplot inset shows charge neutrality point dispersion (center line, median; box limits, upper and
 97 lower quartiles). **e,** Leakage current (I_{gs}) of all gSGFETs in the array throughout the voltage sweep. **f,** Transfer
 98 curve (blue squares and line) and its first derivative (transconductance (g_m), black line) of a gSGFET. **g,**
 99 Frequency response of the transconductance at two different points of the transfer curve (f): V_{gs} lower than the
 100 CNP (green), where g_m is negative resulting in a signal inversion (180° phase); and V_{gs} higher than the CNP
 101 (orange), where g_m is positive and thus results in no inversion (0° phase). Independently of the branch of the
 102 transfer curve where a gSGFET is polarized, the module of g_m is similar to the steady-state value for a wide
 103 bandwidth (~0 - 1 kHz).

104

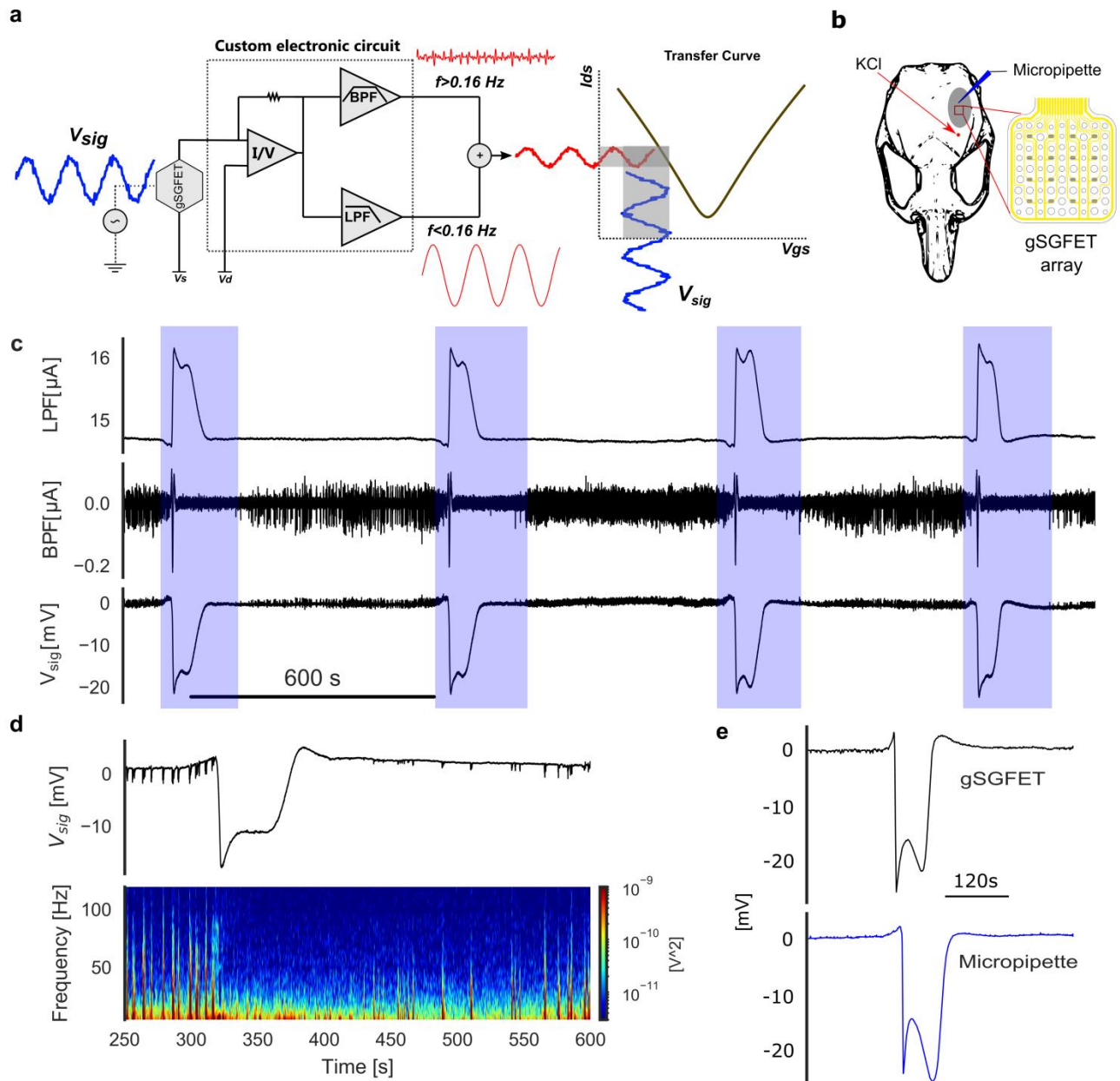


Fig. 2 | Infralow, local field potential, and wide-band *in vivo* gSGFET recordings of cortical spreading depression (CSD). **a**, Schematic of the gSGFET recording setup and signal post processing methodology. The custom electronic circuit is used to perform the *in vivo* characterization (transfer curve) and record the transistor current in the low-pass-filtered (LPF) and the band-pass-filtered (BPF) bands. From the combination of both signals and taking into account the current-to-voltage conversion, the calibrated wide-band signal (V_{sig}) is obtained. **b**, Schematic of a rat skull depicting the craniotomy (grey area), the location of the gSGFET array and micropipette as also the frontal craniotomy where 5mM KCl was applied to induce CSDs. **c**, Electrophysiological recordings obtained with a gSGFET epicortical array during the induction of four CSD events (blue shade). From top to bottom: LPF signal, BPF and voltage-converted wide-band signal. **d**, Voltage-converted wide-band signal of a CSD event recorded by a gSGFET and spectrogram showing the characteristic silencing of activity. **e**, Comparison of a CSD signal recorded by a graphene transistor and a solution-filled glass micropipette with a Ag/AgCl wire demonstrating the excellent similarity in shape, magnitude and time span.

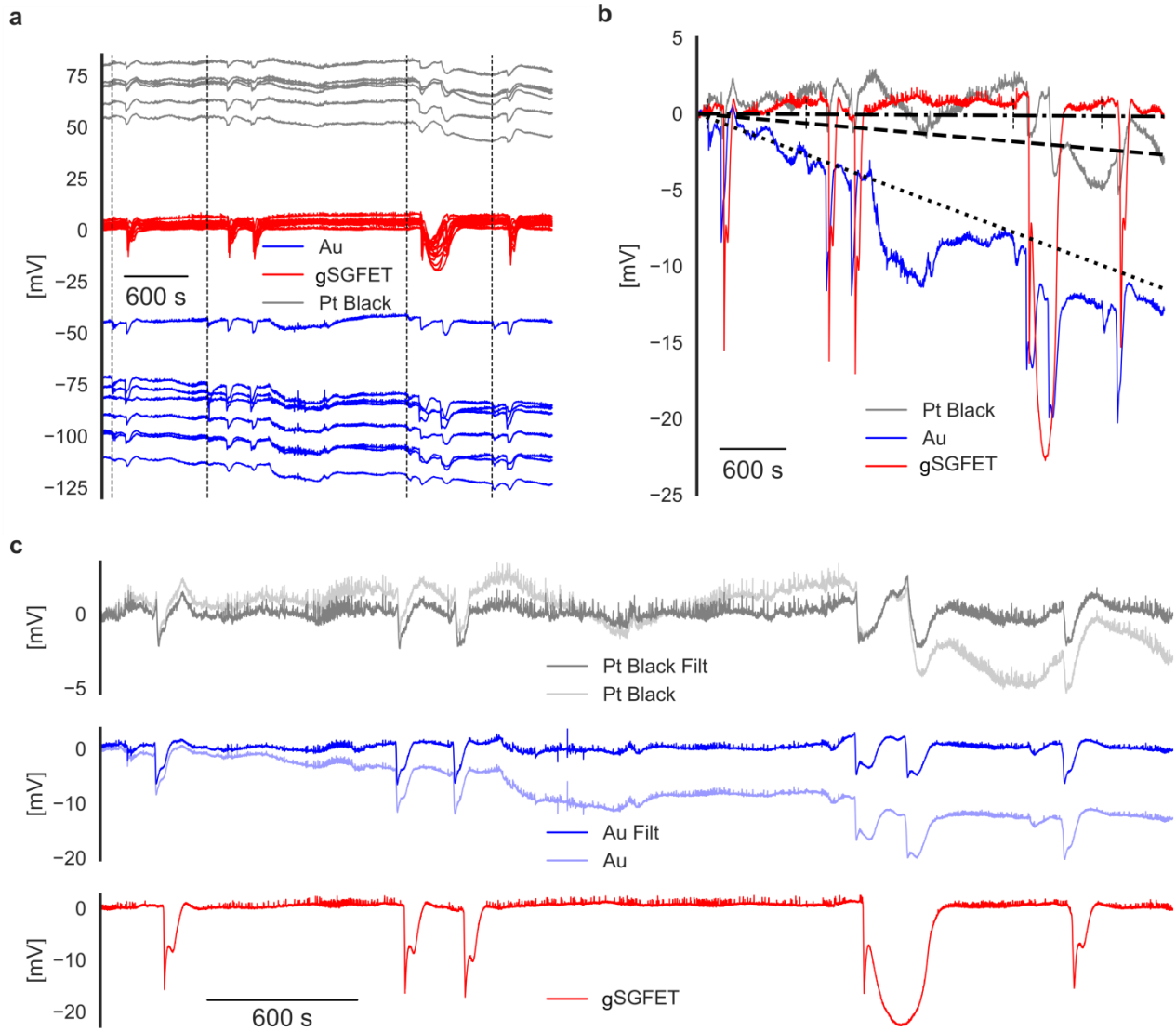
120 ***In vivo* wide-band recordings with gSGFETs**

121 Cortical spreading depression^{10,12,19} was chosen to illustrate the capabilities of graphene transistors to
122 record electrophysiological signals in a wide bandwidth. Experimentally, two craniotomies were
123 performed over the left hemisphere of isoflurane-anaesthetized Wistar rats: a larger craniotomy over
124 the primary somatosensory cortex, where the epicortical probe was placed, and a smaller one in the
125 frontal cortex, where 5 mM KCl was applied locally to induce CSD (Fig. 2b). A custom electronic
126 circuit allowed us to simultaneously record at two frequency bands: low-pass filtered band (LPF, ≈ 0 -
127 0.16 Hz) and band-pass filtered band (BPF, 0.16 Hz-10 kHz) with different gains (10^4 , and 10^6
128 respectively) to avoid amplifier saturation due to the high-amplitude CSD signal. In a first set of
129 experiments, we recorded the LPF and BPF signals with an epicortical gSGFET array during the
130 induction of CSD events (Fig. 2c). The graphene transistors were polarized in the hole conduction
131 regime, i.e. $V_{gs} < \text{CNP}$ (negative g_m) resulting in an inversion of the recorded LPF and BPF current
132 signals with respect to the voltage signal occurring at the gate. The LPF signal shows the very slow
133 CSD event whereas the BPF signal corresponds to the local field potential, revealing the silencing of
134 activity characteristic of cortical spreading depression. It is important to note that the high frequency
135 content of the steep depolarization seen in the BPF signal at the beginning of each CSD event is
136 generally the unique information of the CSD seen in AC-coupled recordings. After calibration the
137 wide-band electrophysiological signal can be obtained (see Fig. 2 a, c and Data Analysis section in
138 Methods). The calibration procedure eliminates both the variations associated with the different
139 current levels and the transconductance differences at the bias point between the transistors (Fig. S1).
140 In each CSD event a small positive shift of 1-2 mV generally precedes the depression, immediately
141 after which a steep negative change (≈ -20 mV) can be observed, which slowly recovers during the
142 next minute or so. The CSD-associated silencing of high-frequency activity and its progressive
143 recovery is shown in the voltage wave and spectrogram of Fig. 2d. In order to confirm the fidelity of
144 the CSD recordings of the gSGFET technology, simultaneous recordings with a solution-filled glass
145 micropipette with a Ag/AgCl wire were conducted. The infraslow deflection associated with CSD as
146 measured by gSGFETs has a very similar shape, magnitude and temporal duration than the signal
147 recorded by a micropipette (see Fig. 2e and Fig. S2: cross-correlation = 0.85 ± 0.1 for the recording of
148 two CSD events).

149 **ISA recording capabilities with gSGFETs and microelectrodes**

150 A second set of experiments was designed to compare the performance of gSGFETs with
151 microelectrodes in *in-vivo* direct-coupled recordings. CSD was induced and simultaneously recorded
152 with an gSGFET epicortical array located more posterior to a neural probe containing groups of
153 triodes of 50 μm diameter gold microelectrodes 200 μm apart in which one microelectrode of each
154 triode was modified by deposition of platinum black to lower its impedance (Fig. S3). Data shown in
155 Fig. 3 corresponds to a representative experiment of $n=3$ independent subjects. Fig. 3a shows that
156 gold and platinum black recordings exhibit very large and diverse baseline offsets as well as
157 oscillations and drifts (-7.9 ± 3.3 mV/h, $n=10$ and -3.6 ± 1.6 mV/h, $n=6$), while the gSGFET signals
158 are very stable (1.1 ± 1.0 mV/h, $n=15$). Importantly, gSGFETs record significantly higher amplitudes
159 for the CSD events (-13.3 ± 1.8 mV) in comparison with gold (-4.7 ± 1.6 mV) and platinum black (-

160 3.0 ± 0.7 mV) microelectrodes. Figure 3b highlights one of the intrinsic limitations of microelectrode
 161 technology for the measurement of ISA: polarization-induced drift.



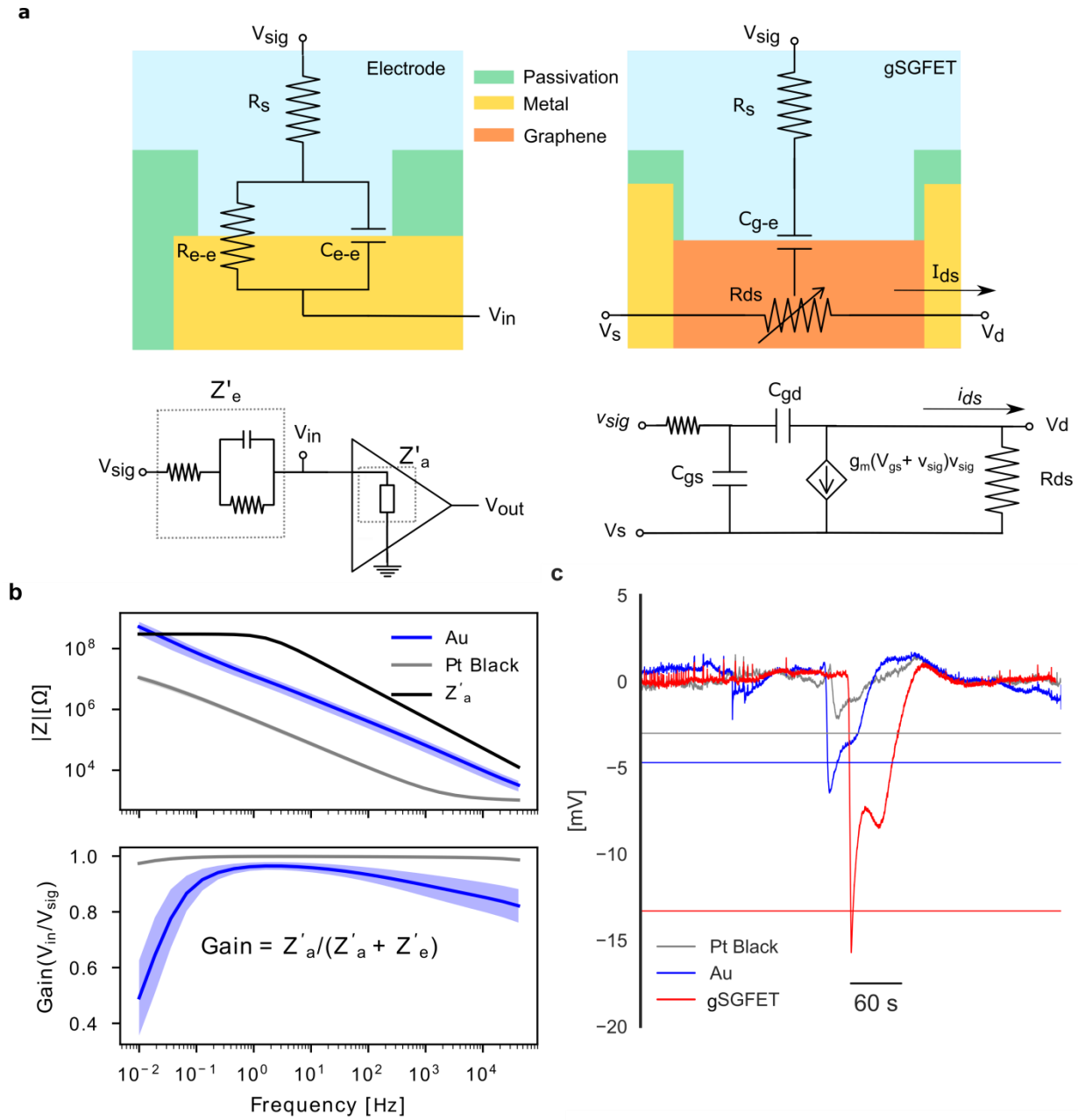
162
 163 **Fig. 3 | Comparison of DC-coupled gSGFET and microelectrode recordings of cortical spreading**
 164 **depression. a-c,** Representative data of one of a total of three independent experiments. **a,** Direct-coupled
 165 recordings of 100 x 50 μm² gSGFET transistors and gold and platinum black 50 μm diameter microelectrodes.
 166 The vertical dashed lines show the time when KCl (5 mM) was applied to induce a CSD. **b,** DC-offset
 167 removed recordings of a representative channel of each type. Black lines illustrate the mean drift: dotted and
 168 dashed correspond to gold and platinum black microelectrodes, respectively, and the dash-dotted line
 169 corresponds to gSGFETs. **c,** DC-offset removed recordings of a representative channel of each type and the
 170 same signal filtered at 0.002 Hz to remove oscillations and drift; the gSGFET signal does not require any
 171 filtering and is therefore not distorted.

172 The drift of the baseline potential superimposed over the huge voltage offsets is problematic as it can
 173 lead to saturation of the amplifiers used to record the signal. More importantly, baseline oscillations
 174 in the infralow frequencies, will potentially hamper the determination of the exact characteristics of
 175 CSD, such as amplitude or waveform, as the required high-pass filter used to remove such effects

will alter the signal shape (see Fig.3c and Fig. S4). Another intrinsic limitation of microelectrode technology is based on the relation between the microelectrode impedance and the input impedance of the recording equipment (Z'_e and Z'_a , respectively)^{21,23}. The recorded signal (V_{in}) is determined by the voltage divider formed by both impedances:

$$V_{in}(f) = I(f)Z'_a(f) = \frac{V_{sig}(f) Z'_a(f)}{Z'_a(f) + Z'_e(f)} \quad (1)$$

Eq. (1) implies that when Z'_a is not substantially larger than Z'_e , the recorded signals will be attenuated and shifted with respect to V_{sig} ²². It is important to highlight that the $Z'_a \gg Z'_e$ requirement to achieve a voltage gain equal to 1 could be compromised, especially at very-low frequencies, when the electrode area is scaled down, due to the inverse relation between electrode impedance and its area, leading to high-pass filtering of the recorded signals. By measuring the impedance of both electrode types and modelling the preamplifier impedance with the values reported by the manufacturer, we obtained the voltage gain (V_{in}/V_{sig}) of the equivalent circuit formed by the recording electrode and the amplifier, see Fig. 4a-b. Fig. 4c shows a representative CSD recorded by a gSGFET and gold and platinum black microelectrodes and the mean amplitude of the first peak for each type. For the 50 μm diameter gold microelectrodes, an attenuation lower than 50% is expected from Fig. 4b, which is in agreement with the experimental results. For the platinum black electrodes we tentatively attribute the higher than predicted attenuation to *in vivo* electrochemical processes that impact the electrode response at very low frequencies³³. We assign the superior performance of gSGFETs to the following main reasons. First, graphene exhibits an excellent DC stability, as demonstrated by low *in vivo* drift. We attribute this to the low density of states of pristine graphene near the Fermi level, which decreases the overall electronic overlap with redox species³⁴, and to the low density of extrinsic electron transfer sites, i.e. defects and edges, all contributing to the excellent electrochemical inertness of CVD graphene^{24,35,36}. The low leakage current measured (Fig. 1e) also supports the electrochemical inertness.



199

Fig. 4 | Microelectrode and gSGFET recording modes: considerations for infraslow recordings. **a**, Cross-sectional view and superimposed electric equivalent circuit models of a recording electrode and a gSGFET. For an electrode, the electrode-electrolyte interface, is modelled simply as a capacitor and a resistor in parallel (R_{e-e} , C_{e-e}). V_{in} , the voltage at the input of the amplifier is determined by the voltage divider formed by Z'_e and Z'_a , the effective electrode and amplifier impedance, respectively. R_s represents the electrolyte resistance. In the case of a gSGFET, V_{sig} modulates the graphene channel resistance (R_{ds}) by field-effect through the gate capacitance (C_{g-e}), which results in current variations (i_{ds}) proportional to the transconductance value at the bias point, plus the voltage signal (which is mostly negligible for small amplitude electrophysiological signals), as seen in the small signal model. **b**, Mean and standard deviation of the impedance module (experimental data) of nine 50 μm diameter gold (blue) and six platinum black (grey) microelectrodes together with Z'_a and calculated voltage gain (V_{in}/V_{sig}) for each microelectrode type. **c**, Recordings of a CSD event for each type of microelectrodes and a gSGFET. Horizontal lines represent the mean value of CSD amplitude.

212 The second reason why graphene microtransistors can record infraslow signals is related to their
 213 working mechanism, which is significantly different from that of electrodes. In gSGFETs, voltage
 214 oscillations near the active graphene channel modulate the current flow along it (see schematic and
 215 small-signal model in Fig. 4a). Eq. 2 shows the relation between the recorded current (I_{ds-rec}) and
 216 the signal (V_{sig}):

$$I_{ds-rec}(V_{gs}, V_{sig}) = I_{ds}(V_{gs}) + i_{ds}(V_{gs}, V_{sig}) = I_{ds}(V_{gs}) + g_m (V_{gs} + V_{sig}) V_{sig}, \quad (2)$$

217 where I_{ds} is the current at the bias point V_{gs} and i_{ds} the current variation induced by the gate signal.
 218 This equation is valid and frequency-independent as long as g_m is also frequency-independent. In
 219 this work (Fig. 1g), we provide evidence that the transconductance of gSGFETs remains constant in a
 220 wide bandwidth and that this behaviour is preserved with further downscaling of gSGFETs
 221 (Fig.S5).

222 Mapping cortical spreading depression with gSGFETs

223 As an example of the potential of gSGFET technology, we mapped the propagation of CSD events
 224 using a 4x4 epicortical gSGFET array and compared the signals with what is observed in
 225 conventional high-pass filtered recordings (Fig. 5a-b). The recording of the CSD event with the
 226 gSGFET array reveals that while the onset of the negative shift is similar for all gSGFETs, there is
 227 much more variety in the subsequent recovery, with some transistors exhibiting a second negative
 228 shift with higher amplitude than the first one. This effect can also be observed in the last two frames
 229 (corresponding to 80 s and 90 s) of the spatial maps of gSGFET recordings (Fig. 5b) where recovered
 230 and still depressed brain areas coexist. Importantly, this information is lost in conventional
 231 microelectrode recordings, where only the CSD onset is observed due to the high pass filter in the
 232 recording electronics. We found that the mean duration of CSD events is 47 ± 8 s and a speed of
 233 propagation of 8 ± 1 mm/min (n=10 CSDs collected from two different subjects).

234 Under physiological conditions, there is a neurovascular response, vasodilatation and increased
 235 regional cerebral blood flow (rCBF) due to spreading depolarization that causes spreading
 236 hyperemia¹⁰. However, most studies on CSD neurovascular coupling have been performed with
 237 mapping techniques for the rCBF while electrical activity is measured only at two sites with glass
 238 micropipettes⁵. Here, taking advantage of the gSGFET technology, we designed an experiment in
 239 which we could simultaneously map both variables. Fig. 5c provides further evidence of the
 240 spreading depolarization and hyperemia neurovascular coupling. We used a non-contact, wide-field
 241 technique, laser speckle contrast imaging (LSCI)³⁷, that allows imaging variations of rCBF³⁸.
 242 Experimentally, a craniotomy was performed in a Wistar rat and a continuous-wave temperature
 243 controlled laser diode and a camera were mounted to image a wide area inside in which an epicortical
 244 16-channel gSGFET array was placed. After 5mM KCl administration, CSD was induced, which was
 245 followed by an increase in rCBF that slowly returned (4-5minutes) to basal values (Fig. 5c).

246 We also performed *in vivo* experiments with intracortical probes consisting of a linear array of 15
 247 gSGFETs spanning the entire depth of a rat cortex (Fig. 6a). From both the ordered recording and the
 248 spatiotemporal voltage map (Fig. 6b), it can be seen how CSD occurs in the whole cortex depth. A

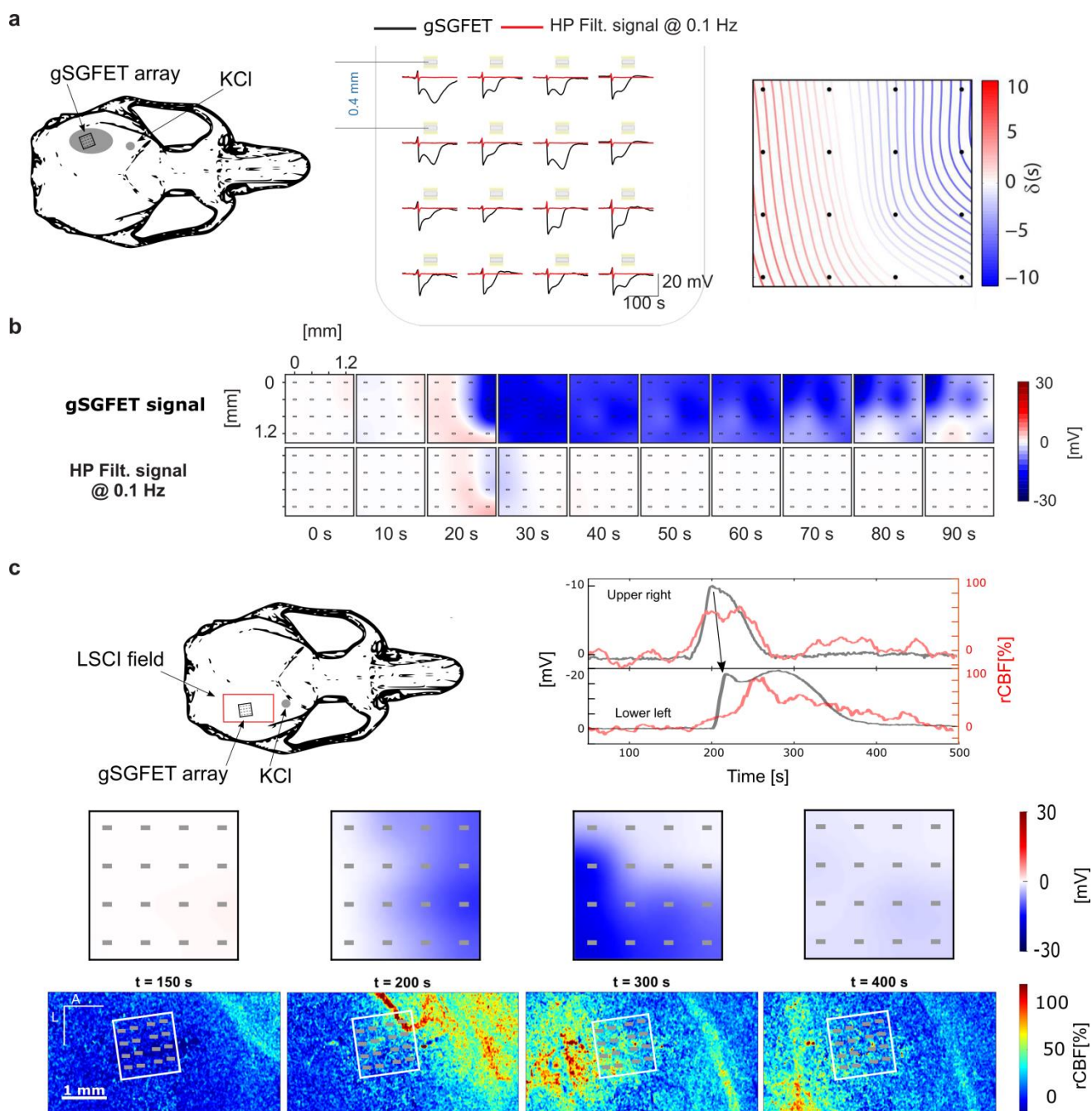
249 transition from a superficial long depolarization to a shorter one preceded and followed by a
250 hyperpolarization in the deeper layers can be clearly observed.

251 **Outlook**

252 In this work we show that gSGFETs can record neural signals in a wide electrophysiological
253 bandwidth, from infralow (<0.1 Hz) frequencies to the typical local field potential bandwidth, similar
254 to solution-filled glass micropipettes but with the capability of overcoming their spatial sampling
255 limitations. Importantly, this capability does not depend on a given transistor size but is preserved
256 among a wide range of device sizes, which brings freedom when designing an array for a given
257 application. There are two main reasons that explain this unique recording capability: the direct DC-
258 coupling of transistors, in contrast to standard passive electrodes; and the excellent electrochemical
259 stability of graphene. Making use of these features, gSGFET technology opens the possibility of
260 mapping infralow oscillations with high fidelity and spatial resolution (epicortically and
261 intracortically). This can lead to a better understanding of the brain regions where ISA is initiated, its
262 propagation to other areas and a clarification of the interplay of different cellular types, which are
263 still poorly understood^{1,2,39}. Additionally, the wide recording bandwidth of gSGFETs can help in
264 determining the relation between ISA and higher frequency signals^{17,40} and contribute to a better
265 understanding of the genesis of local field potentials⁴¹ and of cortical wave propagation features^{42,43}.

266 Since 2014, work exploiting both the transparency and electrical conductivity of graphene has
267 allowed simultaneous local field potential recordings using graphene microelectrodes, and imaging or
268 optical stimulation at the same position, which has profound implications in neuroscience^{24,44}. Our
269 work demonstrates that graphene transistors can be used together with imaging techniques, such as
270 LSCI to map infralow electrophysiological signals and regional cerebral blood flow. This
271 combination of techniques holds great potential and can contribute to a better understanding of
272 neurovascular coupling phenomena.

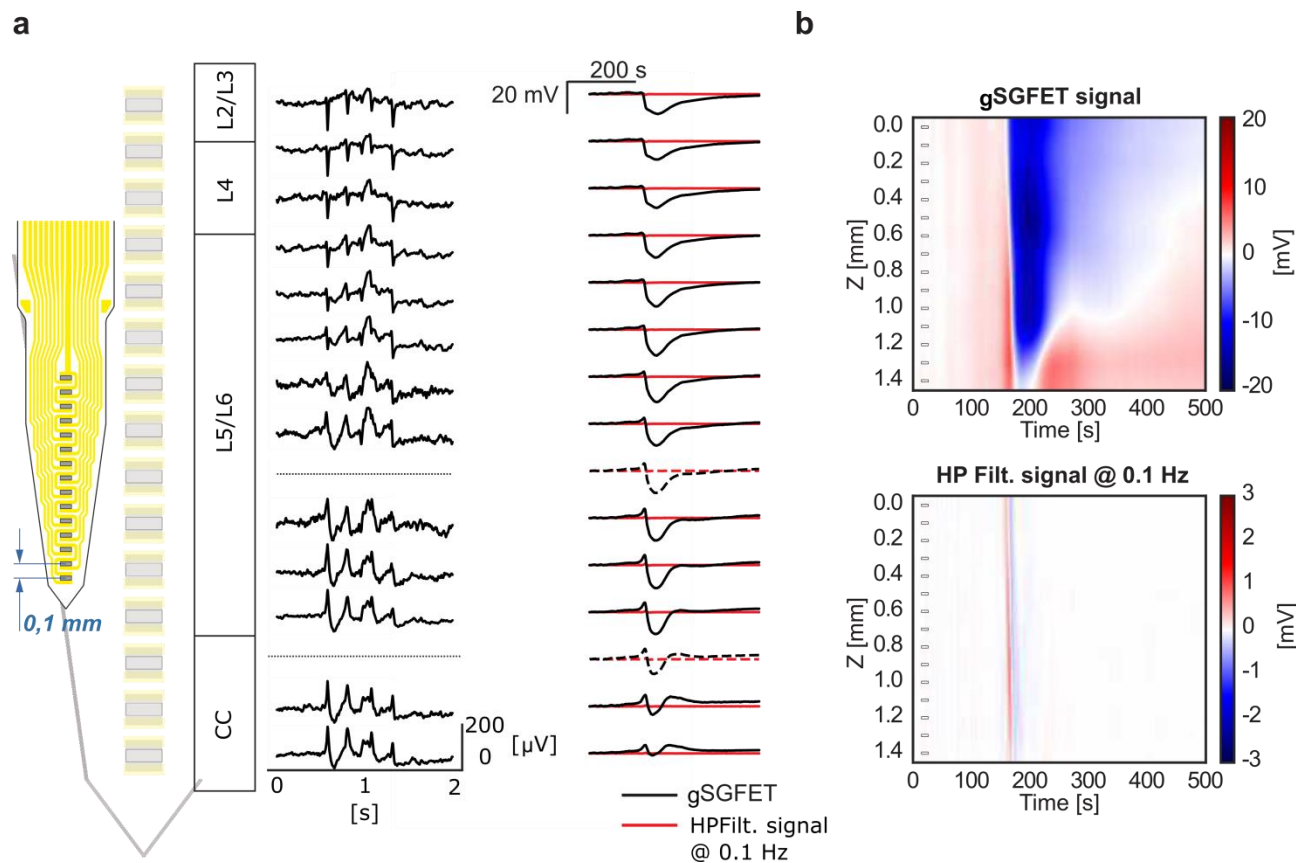
273



274

275 **Fig. 5 | Mapping cortical spreading depression with graphene transistors.** **a**, Infralow frequency signals
 276 recorded by a 4x4, 400 μm grid spacing, gSGFET array (black lines) during the occurrence of a CSD event as
 277 illustrated in the top left schematic. The contour plot shows the time delays of the onset of CSD with respect to
 278 the mean time illustrating the spatiotemporal course of the CSD. **b**, Interpolated spatial voltage maps showing
 279 the propagation of the same CSD event as measured by the gSGFET array. **a,b** High pass filtered recordings at
 280 0.1Hz (red lines in **a** and bottom spatial voltage maps in **b**) are included to illustrate the loss of signal
 281 information in conventional microelectrode recordings. **c**, Schematic of a rat skull depicting the laser speckle
 282 contrast imaging field-of-view and the position of the gSGFET array. Electrical recordings and optical
 283 imaging were performed directly on the cortical surface. Time evolution of the upper right and lower left
 284 graphene microtransistors as well as the regional cerebral blood flow (rCBF) measured at the same position
 285 showing their co-occurrence. Colour maps represent the spatial value of the extracellular voltage as measured

286 by the gSGFET array (top) and the rCBF (bottom) at a given set of times after the induction of a CSD event.
 287 Representative data of one of a total of two independent experiments.



288
 289 **Fig. 6 | Depth profile of the infralow-frequency voltage variations induced by cortical spreading**
 290 **depression in a rat cortex. a**, Layout of the fabricated 15-channel graphene intracortical probe and
 291 ordered local field potential recordings. Infralow-frequency recordings (black lines) during the
 292 occurrence of a CSD event. Dashed lines, have been interpolated from nearby transistors. Depth
 293 position is indicated by the layer number and corpus callosum (CC). **b**, Colour maps of the temporal
 294 course of the infralow changes during a CSD event across the depth of a rat cortex. **a-b**, Same signal
 295 high-pass filtered at 0.1 Hz (red lines) and their spatio-temporal colour map are included to illustrate
 296 the loss of information in conventional microelectrode recordings.

297 In the particular case of CSD, where no non-invasive electrophysiological technique has been
 298 demonstrated capable of its monitoring, the adoption of invasive DC-coupled electrode recordings
 299 has been proposed to provide further diagnostic information and easy and direct detection of CSDs¹³.
 300 gSGFET technology emerges as a potential preclinical as well as clinically relevant tool to help
 301 determine the relation of CSDs to neural disorders such as migraine, malignant stroke, subarachnoid
 302 and intracranial haemorrhage, and traumatic brain injury. If the challenges of translating gSGFET
 303 technology to the clinics, such as chronic and safe operation and human compatibility are surpassed,
 304 gSGFETs could be applied in neurointensive care monitoring^{12,14} or for CSD intraoperative
 305 monitoring since there is evidence that CSD can occur during neurosurgical procedures⁴⁵.
 306 Importantly, in contrast to electrodes where a signal is needed to measure electrode impedance, the
 307 possibility to measure the characteristic transfer curve of a gSGFET *in vivo* at any time, allows
 308 assessing the stability as well as the signal coupling magnitude (transconductance) during an implant

lifetime, therefore easing the evaluation of its chronic performance. In summary, our work demonstrates that gSGFET arrays are ideal candidates to fill the gap of a large-scale, high-spatiotemporal recording technology that covers a wide electrophysiological bandwidth in a potentially fully implantable, nontoxic, clinical-scale device. By measuring the full bandwidth of brain activity with high spatiotemporal resolution we will be able to improve our understanding of brain function in health and disease status, and develop better diagnostic and therapeutic procedures for those affected.

References

- 1 Hughes, S. W., Lörincz, M. L., Parri, H. R. & Crunelli, V. in *Progress in Brain Research* Vol. 193 (eds Eus J. W. Van Someren *et al.*) 145-162 (Elsevier, 2011).
- 2 Mitra, A. *et al.* Spontaneous Infra-slow Brain Activity Has Unique Spatiotemporal Dynamics and Laminar Structure. *Neuron*, doi:<https://doi.org/10.1016/j.neuron.2018.03.015>.
- 3 Lecci, S. *et al.* Coordinated infraslow neural and cardiac oscillations mark fragility and offline periods in mammalian sleep. *Science Advances* **3**, e1602026 (2017).
- 4 Mitra, A., Snyder, A. Z., Tagliazucchi, E., Laufs, H. & Raichle, M. E. Propagated infra-slow intrinsic brain activity reorganizes across wake and slow wave sleep. *Elife* **4** (2015).
- 5 Hiltunen, T. *et al.* Infra-slow EEG fluctuations are correlated with resting-state network dynamics in fMRI. *Journal of Neuroscience* **34**, 356-362 (2014).
- 6 Leopold, D. A., Murayama, Y. & Logothetis, N. K. Very slow activity fluctuations in monkey visual cortex: implications for functional brain imaging. *Cerebral cortex* **13**, 422-433 (2003).
- 7 Kelly, A. C., Uddin, L. Q., Biswal, B. B., Castellanos, F. X. & Milham, M. P. Competition between functional brain networks mediates behavioral variability. *Neuroimage* **39**, 527-537 (2008).
- 8 Chung, D. Y. & Ayata, C. in *Primer on Cerebrovascular Diseases (Second Edition)* (eds José Biller *et al.*) 149-153 (Academic Press, 2017).
- 9 Hartings, J. A. *et al.* The continuum of spreading depolarizations in acute cortical lesion development: examining Leão's legacy. *Journal of Cerebral Blood Flow & Metabolism* **37**, 1571-1594 (2017).
- 10 Dreier, J. P. The role of spreading depression, spreading depolarization and spreading ischemia in neurological disease. *Nat Med* **17**, 439-447 (2011).
- 11 Dreier, Jens P. & Reiffurth, C. The Stroke-Migraine Depolarization Continuum. *Neuron* **86**, 902-922, doi:<https://doi.org/10.1016/j.neuron.2015.04.004> (2015).
- 12 Lauritzen, M. *et al.* Clinical relevance of cortical spreading depression in neurological disorders: migraine, malignant stroke, subarachnoid and intracranial hemorrhage, and traumatic brain injury. *Journal of Cerebral Blood Flow & Metabolism* **31**, 17-35 (2011).
- 13 Hartings, J. A. *et al.* Direct current electrocorticography for clinical neuromonitoring of spreading depolarizations. *Journal of Cerebral Blood Flow & Metabolism* **37**, 1857-1870 (2017).

- 347 14 Dreier, J. P. *et al.* Recording, analysis, and interpretation of spreading depolarizations in
348 neurointensive care: review and recommendations of the COSBID research group. *Journal of*
349 *Cerebral Blood Flow & Metabolism*, 0271678X16654496 (2016).
- 350 15 Kovac, S., Speckmann, E.-J. & Gorji, A. Uncensored EEG: The role of DC potentials in
351 neurobiology of the brain. *Progress in Neurobiology*,
352 doi:<https://doi.org/10.1016/j.pneurobio.2018.02.001> (2018).
- 353 16 Vanhatalo, S., Voipio, J. & Kaila, K. Full-band EEG (FbEEG): an emerging standard in
354 electroencephalography. *Clinical Neurophysiology* **116**, 1-8,
355 doi:<http://dx.doi.org/10.1016/j.clinph.2004.09.015> (2005).
- 356 17 Vanhatalo, S. *et al.* Infraslow oscillations modulate excitability and interictal epileptic activity
357 in the human cortex during sleep. *Proceedings of the National Academy of Sciences of the*
358 *United States of America* **101**, 5053-5057 (2004).
- 359 18 Hofmeijer, J. *et al.* Detecting Cortical Spreading Depolarization with Full Band Scalp
360 Electroencephalography: An Illusion? *Frontiers in Neurology* **9**,
361 doi:10.3389/fneur.2018.00017 (2018).
- 362 19 Ayata, C. & Lauritzen, M. Spreading depression, spreading depolarizations, and the cerebral
363 vasculature. *Physiological reviews* **95**, 953-993 (2015).
- 364 20 Stensaas, S. S. & Stensaas, L. J. Histopathological evaluation of materials implanted in the
365 cerebral cortex. *Acta Neuropathologica* **41**, 145-155, doi:10.1007/bf00689766 (1978).
- 366 21 Li, C. *et al.* Evaluation of microelectrode materials for direct-current electrocorticography.
367 *Journal of neural engineering* **13**, 016008 (2015).
- 368 22 Nelson, M. J., Pouget, P., Nilsen, E. A., Patten, C. D. & Schall, J. D. Review of signal
369 distortion through metal microelectrode recording circuits and filters. *Journal of neuroscience*
370 *methods* **169**, 141-157 (2008).
- 371 23 Stacey, W. C. *et al.* Potential for unreliable interpretation of EEG recorded with
372 microelectrodes. *Epilepsia* **54**, 1391-1401 (2013).
- 373 24 Kuzum, D. *et al.* Transparent and flexible low noise graphene electrodes for simultaneous
374 electrophysiology and neuroimaging. *Nature communications* **5**, 5259 (2014).
- 375 25 Deneux, T. *et al.* Accurate spike estimation from noisy calcium signals for ultrafast three-
376 dimensional imaging of large neuronal populations in vivo. *Nature Communications* **7**,
377 12190, doi:10.1038/ncomms12190
378 <https://www.nature.com/articles/ncomms12190#supplementary-information> (2016).
- 379 26 Fang, H. *et al.* Capacitively coupled arrays of multiplexed flexible silicon transistors for long-
380 term cardiac electrophysiology. *Nature biomedical engineering* **1**, 0038 (2017).
- 381 27 Heremans, P. *et al.* Mechanical and electronic properties of thin-film transistors on plastic,
382 and their integration in flexible electronic applications. *Advanced Materials* **28**, 4266-4282
383 (2016).
- 384 28 Hess, L. H., Seifert, M. & Garrido, J. A. Graphene transistors for bioelectronics. *Proceedings*
385 *of the IEEE* **101**, 1780-1792 (2013).
- 386 29 Kim, B. J. *et al.* High-Performance Flexible Graphene Field Effect Transistors with Ion Gel
387 Gate Dielectrics. *Nano Letters* **10**, 3464-3466, doi:10.1021/nl101559n (2010).

388 30 Kostarelos, K., Vincent, M., Hebert, C. & Garrido, J. A. Graphene in the Design and
389 Engineering of Next-Generation Neural Interfaces. *Advanced Materials* **29** (2017).

390 31 Benno, M. B. *et al.* Mapping brain activity with flexible graphene micro-transistors. *2D*
391 *Materials* **4**, 025040 (2017).

392 32 Hébert, C. *et al.* Flexible Graphene Solution-Gated Field-Effect Transistors: Efficient
393 Transducers for Micro-Electrocorticography. *Advanced Functional Materials* **28**, 1703976,
394 doi:doi:10.1002/adfm.201703976 (2018).

395 33 Shinwari, M. W. *et al.* Microfabricated Reference Electrodes and their Biosensing
396 Applications. *Sensors* **10**, 1679 (2010).

397 34 Chen, S., Liu, Y. & Chen, J. Heterogeneous electron transfer at nanoscopic electrodes:
398 importance of electronic structures and electric double layers. *Chemical Society Reviews* **43**,
399 5372-5386 (2014).

400 35 Brownson, D. A. & Banks, C. E. The electrochemistry of CVD graphene: progress and
401 prospects. *Physical Chemistry Chemical Physics* **14**, 8264-8281 (2012).

402 36 Brownson, D. A. C., Munro, L. J., Kampouris, D. K. & Banks, C. E. Electrochemistry of
403 graphene: not such a beneficial electrode material? *RSC Advances* **1**, 978,
404 doi:10.1039/c1ra00393c (2011).

405 37 Valdes, C. P. *et al.* Speckle contrast optical spectroscopy, a non-invasive, diffuse optical
406 method for measuring microvascular blood flow in tissue. *Biomedical optics express* **5**, 2769-
407 2784 (2014).

408 38 Boas, D. A. & Dunn, A. K. Laser speckle contrast imaging in biomedical optics. *Journal of*
409 *biomedical optics* **15**, 011109 (2010).

410 39 Shibata, M. & Suzuki, N. Exploring the role of microglia in cortical spreading depression in
411 neurological disease. *Journal of Cerebral Blood Flow & Metabolism* **37**, 1182-1191,
412 doi:10.1177/0271678x17690537 (2017).

413 40 Mitra, A. & Raichle, M. E. How networks communicate: propagation patterns in spontaneous
414 brain activity. *Phil. Trans. R. Soc. B* **371**, 20150546 (2016).

415 41 Herreras, O. Local field potentials: myths and misunderstandings. *Frontiers in neural circuits*
416 **10**, 101 (2016).

417 42 Massimini, M., Huber, R., Ferrarelli, F., Hill, S. & Tononi, G. The sleep slow oscillation as a
418 traveling wave. *Journal of Neuroscience* **24**, 6862-6870 (2004).

419 43 Capone, C. *et al.* Slow Waves in Cortical Slices: How Spontaneous Activity is Shaped by
420 Laminar Structure. *Cerebral Cortex*, 1-17 (2017).

421 44 Park, D.-W. *et al.* Graphene-based carbon-layered electrode array technology for neural
422 imaging and optogenetic applications. *Nature communications* **5**, ncomms6258 (2014).

423 45 Carlson, A. P. *et al.* Cortical spreading depression occurs during elective neurosurgical
424 procedures. *Journal of neurosurgery* **126**, 266-273 (2017).

425

426

427 Acknowledgments

428 This work was funded by the European Union's Horizon 2020 research and innovation programme
429 under Grant Agreement No. 696656 (Graphene Flagship) and No. 732032 (BrainCom). This work
430 has made use of the Spanish ICTS Network MICRONANOFABS partially supported by MINECO
431 and the ICTS 'NANBIOSIS', more specifically by the Micro-NanoTechnology Unit of the CIBER in
432 Bioengineering, Biomaterials & Nanomedicine (CIBER-BBN) at the IMB-CNM. E.M.C. worked in
433 this manuscript during the PhD in Electrical and Telecommunication Engineering at the Universitat
434 Autònoma de Barcelona. E. d. C. thanks to Spanish Ministerio de Economía y Competitividad for the
435 Juan de la Cierva postdoctoral grant IJCI-2015-25201. T. Du acknowledges support from Fundació
436 CELLEX Barcelona, Ministerio de Economía y Competitividad /FEDER (PHOTODEMENTIA,
437 DPI2015-64358-C2-1-R), the "Severo Ochoa" Programme for Centres of Excellence in R&D (SEV-
438 2015-0522) and the Obra social "la Caixa" Foundation (LlumMedBcn).

439 Author contributions

440 E.M.C. did most of the fabrication and characterization of the gSGFET arrays, contributed to the
441 design and performance of the *in vivo* experiments, analyzed the data and wrote the manuscript. X.I.
442 designed the neural probes and fabricated the microelectrode arrays. A.B.C. contributed to the
443 fabrication and characterization of the gSGFET arrays. M.D. performed the *in vivo* experiments.
444 P.G., C.H., J.B. and E.P.A. contributed to the growth of the CVD graphene. E.P.A., E.dC. and
445 J.M.dC.S. contributed to the transfer of graphene. E.P.A., E.dC.G. and G.R. contributed to the
446 characterization of CVD graphene. J.M.A. contributed to the fabrication of the custom electronic
447 instrumentation and development of a python-based user interface. A.C. contributed to the CSD
448 propagation analysis. R.G.C. contributed in the noise characterization and analysis of the devices.
449 T.Dr., E.V. and T.Du. contributed to the *in vivo* measurements and analysis of cerebral blood flow.
450 M.D., M.S.V., A.G.B, R.V. and J.A.G. participated in the design of the *in vivo* experiments and
451 thoroughly reviewed the manuscript. A.G.B. contributed in the design and fabrication of the custom
452 electronic instrumentation, development of a custom gSGFET python library and in the analysis of
453 the data. All authors read and reviewed the manuscript.

454 Competing interests

455 Patent application (n° P201831068) filled by CSIC, ICREA, CIBER, ICN2 and IDIBAPS; inventors:
456 A.G.B., E.M.C., X.I., R.V., M.S.V. and J.A.G.; concerning a graphene transistor system for
457 measuring electrophysiological signals (pending).

458 Methods

459 Graphene growth and characterization

460 Graphene layers were grown by Chemical Vapor Deposition (CVD) using one of the following
461 procedures: a) A lamp-heated rapid thermal CVD equipment from Jipelec and 25 μm thick, 99.8 %
462 metal basis copper foil provided by AlfaAesar have been employed. Prior to graphene CVD growth,
463 copper foils were sequentially cleaned in acetic acid and acetone, and finally rinsed in isopropyl
464 alcohol (IPA). Sample dimensions were 6 x 5 cm^2 . Growth processing conditions consisted in 10
465 minutes at 750 $^{\circ}\text{C}$, 200 sccm H_2 plus 5 minutes at 800 $^{\circ}\text{C}$, 25 sccm CH_4 / 200 sccm H_2 . b) Chemical
466 vapour deposition was on a 4.5x7 cm^2 copper foil (Alfa Aesar, annealed, Coated). Prior to the
467 growth, the copper foil was electropolished during 5 min at a fixed current density of 62 mA/cm^{-2} in

a solution containing H₂O (1 L) + H₃PO₄ (0.5 L) + ethanol (0.5 L) + isopropanol (0.1 L) and urea (10 g). Then, the copper foil was loaded in a planar quartz tube (1600x60 mm) and heated by a three zone oven. A first annealing step at 1015 °C under a 400 sccm argon flow at 100 mbar during 1 h was followed by a 15-min growth step at 12 mbar under a gas mixture of 1000 sccm argon, 200 sccm hydrogen and 2 sccm of methane. The sample was then cooled down under a 400 sccm argon flow by removing the quartz tube from the oven. For all samples, a complete Raman characterization was performed using a Witec spectrograph (Fig.S6a-d). Raman maps of 30x30 μm² were registered with a spatial resolution lower than 1 μm² (using a 50x objective). We used a 488 nm excitation wavelength to minimize the copper substrate luminescence signal. The laser power was kept below 1.5 mW to avoid sample heating and a 600 g/nm grating was used to provide a pixel to pixel spectral resolution below 3 cm⁻¹.

gSGFET array fabrication and characterization

Four-inch silicon wafers were used as a support to build the devices. First, a 10-μm-thick polyimide layer (PI-2611, HD MicroSystems) was spin-coated to be used as substrate and hard-baked at 350°C to complete the imidation process. Graphene transistors were fabricated in a sandwich-like structure. For that, a first layer of metal (Ti/Au, 10/100 nm) was evaporated and defined in a standard lift-off process using the image reversal photoresist AZ5214E (Clariant GmbH, Germany). Then, single-layer graphene was transferred by electrochemical delamination⁴⁶. After removing the PMMA protection layer, the graphene active areas were defined by means of an oxygen-based reactive ion etching (RIE). A second metal layer (Ni/Au, 20/200nm) was evaporated and defined in a similar standard lift-off process avoiding the use of ultrasounds in order to maintain graphene integrity. SU-8 (SU-8 2005, MicroChemCorp., USA) a permanent epoxy-based negative photoresist was used to passivate the metal leads while defining the graphene channel and metal contacts. Finally, the polyimide substrate was structured in a deep-RIE process using the thick AZ9260 positive photoresist (Clariant GmbH, Germany) as an etching mask. Polyimide probes were directly peeled off from the wafer and placed in a zero insertion force (ZIF) connector to be interfaced with our custom electronic instrumentation. Current-voltage measurements of graphene transistors were performed in common gate mode with a fixed drain-source voltage (V_{ds} =50 mV) varying the gate-source voltage (V_{gs}) vs. a Ag/AgCl reference electrode in 0.01 M PBS solution. Steady-state was ensured by acquiring only after time derivative of 1 s of current is below 5e-7 A/s. The total leakage current was measured for the whole array and corresponds to the sum of the individual leakage currents of all transistors in the array. The frequency response of the transconductance was measured by applying a sum of sinusoidal signals at the electrolyte solution through the reference electrode and by measuring the modulation of the drain current. The acquired signals were splitted into two bands, low frequencies (≈0-10 Hz) in which drain-source current was simultaneous acquired for all transistors in an array, and higher frequencies (10 Hz-30 kHz) in which each transistor was recorded individually (Fig. S7). Data reporting the root-mean-square gate voltage noise dependence on transistor area is included in Supplementary Figure S8 for a better characterization of current gSGFET technology.

Microelectrode array fabrication and characterization

The flexible microelectrode array was fabricated in polyimide in a very similar process. Here, a Ti/Au (20/200 nm) metal layer was evaporated on a 10 μm-thick polyimide-covered four-inch silicon wafer to define the metal tracks and the microelectrodes, while a second polyimide layer (2 μm thick) was used as the passivation layer. Two subsequent etching steps were used to open, firstly, the microelectrode active areas and, secondly, to structure the polyimide in order to define the probe geometry which is the same as in Illa et. al.⁴⁷. Platinum black was deposited in some electrodes (Fig. S3a) by constant polarization amperometry. A voltage of -0.2V against a Ag/AgCl reference

515 electrode was applied during 15 s. Impedance spectra were measured against a Ag/AgCl reference
516 electrode using a Solartron SI 1260 equipment (Solartron analytical, UK) with 20 mV signal
517 amplitude (Fig. S3b).

518 ***Ethical approval and animal handling***

519 All experimental procedures were conducted in accordance with the European Union guidelines on
520 protection of vertebrates used for experimentation (Directive 2010/63/EU of the European Parliament
521 and of the Council of 22 September 2010) and all experiments were approved by the ethics
522 committee of the Hospital Clinic de Barcelona. Rats were kept under standard conditions (room
523 temperature $23 \pm 1^\circ\text{C}$, 12:12-h light-dark cycle, lights on at 08:00), with food (A04, Harlan, Spain)
524 and water available ad libitum.

525 ***In vivo recordings***

526 Eleven adult male Wistar rats (225-375 g) were used in this study. Animals were deeply
527 anaesthetized with isoflurane (4% induction, 1-3% maintenance) and all pressure and incision points
528 were infiltrated with local anesthetic lidocaine. Once under the surgical plane of anesthesia, animals
529 were transferred to a stereotaxic frame with body temperature constantly monitored and maintained
530 at 37°C by means of a thermal blanket. A craniotomy and durotomy were performed on the left or
531 right hemisphere in order to record with epicortical or intracortical arrays, respectively. Additionally,
532 a craniotomy and durotomy were performed over the prefrontal cortex to topically administer 5 mM
533 KCl to induce cortical spreading depression. The large craniotomy was centred at 43 mm antero-
534 posterior (AP) and 42.5 mm medio-lateral (ML) and was 6 mm AP by 4.5 mm ML in size while the
535 smaller craniotomy, located at 50 mm AP and 42 ML, was 2.5 mm AP by 1.25 mm ML. A Ag/AgCl
536 electrode pellet was inserted in temporal muscle and used as reference both for recordings and for the
537 measurement of the transistors transfer curve. All recording probes, either gSGFETs or
538 microelectrodes, were placed directly on the cortical surface and kept in place by adherence to the
539 tissue (Fig. S9a-b). A custom electronic instrumentation was used (Fig. S10), which provides the
540 current-to-voltage conversion and the bias control for each channel. The instrumentation splits the
541 recorded signals into two bands with different gains: low-pass filtered ($< 0.16\text{ Hz}$, 10^4 gain) and
542 band-pass filtered ($0.16\text{ Hz} < f < 160\text{ kHz}$, 10^6 gain). In the experiments where only the gSGFET
543 array was measured the low-pass filtered signals and bias control was managed by a data acquisition
544 system (National Instruments USB-6353), while the band-pass filtered signals were directly acquired
545 by a commercial electrophysiological recording system consisting of a programmable gain amplifier
546 (Multichannel Systems, GmbH) and digitizer interface (CED 1401 and Spike2 software, Cambridge
547 Electronic Design, UK). The LPF and BPF bands were sampled at 1 Hz and 5 kHz respectively. Prior
548 to the beginning of the recordings, the transfer curve of the gSGFET was measured *in situ* to
549 determine the optimum bias point, generally around -0.1 V of the CNP (Fig. S9c-d).

550 For gSGFETs comparison experiments with microelectrodes and the glass micropipettes with
551 Ag/AgCl wire ($\approx 0.15\text{ M}\Omega$) a total of four subjects was used: two subjects were measured with
552 gSGFETs, microelectrodes and a micropipette, one with gSGFETs and microelectrodes (data from
553 Fig.3) and another one with gSGFETs and a micropipette (data from Fig. 2e, and Fig.S2). A custom
554 Simulink model was used to simultaneously measure graphene transistors through an adapted
555 g.HIamp biosignal amplifier (g.tec medical engineering GmbH, Austria) while microelectrodes and
556 the solution-filled glass micropipette were recorded using an g.USBamp (g.tec medical engineering
557 GmbH, Austria). The same reference electrode was used by both amplifiers and signals were sampled
558 at 4.8 kHz.

559 ***Laser speckle contrast imaging***

For the measurement of the regional cerebral blood flow (rCBF), a laser speckle contrast imaging (LSCI) system was used which consists of a continuous-wave temperature-controlled laser diode (785 nm, Thorlabs, Germany) for homogenous full-field illumination and a charge-coupled device camera (sc640-120fm, Basler, Germany), with an exposure time of 5 ms, which captures the diffused light scattered from the imaging area. The speckle contrast was calculated for the predefined region of interest (ROI) at each pixel in temporal domain over 100 frames, to ensure good signal-to-noise ratio. The statistics of different noise sources³⁷ was accounted for when calculating the speckle contrast. Speckle contrast was then related to a rCBF index (BF) as reported in^{38,48}. Finally, the relative blood flow ($\Delta rCBF$) was calculated as:

$$\Delta rCBF = \frac{BF - BF_B}{BF_B} * 100 [\%]$$

where BF_B corresponds to the basal regional blood flow. Fig. S11 shows the area where LSCI was measured in Fig. 5c.

571 **Data Analysis**

All data were analyzed using Python 2.7 packages (Matplotlib, Numpy and Neo) and the custom library PhyREC. The conversion of the recorded current signals (LPF and BPF) to a voltage signal was performed by summation of both signals and interpolation in the *in vivo* measured transfer curve of the corresponding gSGFET. The transfer curve was always measured, at least, at the beginning and end of every acute experiment, and generally some more transfer curves measurements were performed along the duration of the experiment. Comparison of the evolution of the *in vivo* measured transfer curves was systematically performed during data analysis (see Fig. S12a) to ensure that no significant variations are present and to detect (if there are) any misbehaving transistor. Moreover, all recordings presented in the manuscript have been calibrated with the nearest transfer curve measured (following the procedure shown in Fig. S1) to ensure high fidelity in the voltage-converted signals. For visualization purposes microelectrode recordings were filtered (band-stop, 48-52 Hz) and down sampled at 300Hz. For the propagation analysis, the baseline of the signal was estimated as the mean value of the signal until the positive deflection. We defined the onset of the CSD as the onset of the negative shift and detected it using a threshold (Fig. S13a). We defined the WaveTime of each wave as the mean time of the triggers detected in the 16 transistors and constructed a TimeLagMatrix containing time lags for each channel computed with respect to the WaveTime (Fig. S13c). We interpolated the known time lags with a thin-plate smoothing spline technique (Fig.5a). The velocity of the propagation has been estimated computing the gradient of the TimeLagMatrix on the grid⁴³. To determine the direction of the waves, a vector starting at the point with higher negative delay (leader of the propagation) and pointing to the one with the highest positive delay (follower of the propagation) was transformed into polar coordinates to obtain the angle (Fig. S13b). For the colormaps of Fig. 5b,c and Fig. 6b a bicubic interpolation was performed for visualization purposes.

594 **Reference electrode**

Voltages at drain and source terminals used to operate graphene transistors are referred to the reference electrode. The reference electrode is generally grounded in anaesthetized subjects to ensure stable recordings, since the subject is grounded at many points. However, the requirement of the reference electrode to be grounded is not necessary; provided that the reference electrode is properly positioned in a non-active location and does not have drifts and oscillations that interfere with the recording, a proper operation of the graphene transistor is achieved. Importantly, gSGFETs are less sensitive than microelectrode technology to the baseline drift associated with the reference electrode.

Commonly, baseline drift can lead to saturation of the amplifiers used for microelectrode DC-coupled recordings, while the operation principle of graphene transistors does not lead to saturation. The drift of the reference electrode shifts the biasing point which could lead to non-optimal performance of gSGFETs. However, this can be easily solved by changing the transistor bias to the new optimal value, which can be obtained from measuring an in vivo transfer curve.

Code Availability

Custom code developed for neurophysiological analysis of gSGFET signals is available at: <https://github.com/aguimera/PhyREC>.

Data Availability

The experimental data that support the figures within this paper and other findings of this study can be accessed by contacting the corresponding authors. Authors can make data available on request, agreeing on data formats needed.

Methods References

- Valdes, C. P. *et al.* Speckle contrast optical spectroscopy, a non-invasive, diffuse optical method for measuring microvascular blood flow in tissue. *Biomedical optics express* **5**, 2769-2784 (2014).
- Boas, D. A. & Dunn, A. K. Laser speckle contrast imaging in biomedical optics. *Journal of biomedical optics* **15**, 011109 (2010).
- Capone, C. *et al.* Slow Waves in Cortical Slices: How Spontaneous Activity is Shaped by Laminar Structure. *Cerebral Cortex*, 1-17 (2017).
- de la Rosa, C. J. L. *et al.* Frame assisted H₂O electrolysis induced H₂ bubbling transfer of large area graphene grown by chemical vapor deposition on Cu. *Applied Physics Letters* **102**, 022101-022104 (2013).
- Illa, X., Rebollo, B., Gabriel, G., Sánchez-Vives, M. V. & Villa, R. in *SPIE Microtechnologies*. 951803-951803-951806 (International Society for Optics and Photonics).
- Bandyopadhyay, R., Gittings, A., Suh, S., Dixon, P. & Durian, D. J. Speckle-visibility spectroscopy: A tool to study time-varying dynamics. *Review of scientific instruments* **76**, 093110 (2005).